Clear-sky convergence and the origin of tropical congestus clouds

Francisco E. Spaulding-Astudillo [ID][1] and Jonathan L. Mitchell [ID][2, 1]

[1]*Department of Earth, Planetary, and Space Sciences, University of California, Los Angeles*
595 Charles E Young Dr E, Los Angeles, CA 90095, USA
[2]*Department of Atmospheric and Oceanic Sciences, University of California, Los Angeles*
520 Portola Plaza, Los Angeles, CA 90095, USA

ABSTRACT

Congestus clouds, characterized by their vertical extent into the middle troposphere, are widespread in tropical regions and play an important role in Earth's climate system by their contribution to cloud radiative forcing, atmospheric humidification, and surface rainfall. However, their spatial distribution – in particular the abundance of stratiform clouds sourced by the outflow from congestus cloud tops – is inaccurately captured by state-of-the-art climate models, suggesting that fundamental questions regarding their formation, dynamics, and climate impact remain unanswered. Here, we demonstrate the existence of a clear-sky water vapor absorption feature that lends insight into how congestus cloud tops form by detraining preferentially at altitudes between 5-6 km and why they are more prevalent in dry mid-tropospheric conditions. Convective detrainment maximizes at a height of 5-6 km due to a swift decline in radiative cooling in clear-sky regions. This decline is, in turn, a consequence of the absorption feature: more specifically, a non-uniform density of strong absorption lines in the water vapor rotation band. The increased prevalence of congestus clouds in drier mid-tropospheric conditions may be due to stronger vertical gradients in the clear-sky cooling rate, which lead to stronger outflow at 5-6 km. We speculate that, in partnership with stability and entrainment, radiation could significantly and systematically influence mid-tropospheric buoyancy and therefore congestus cloud top formation.

Keywords: Radiative transfer (1335) — Atmospheric clouds (2180) — Atmospheric dynamics (2300)

1. INTRODUCTION

There is a clear need to better understand cloudiness in varied environmental and dynamical conditions on Earth because clouds are crucial to the atmospheric energy and moisture budgets. In fact, clouds remain the largest source of uncertainty in estimates of Earth's climate sensitivity to anthropogenic carbon dioxide emissions (Sherwood et al. 2020; Ceppi & Nowack 2021). Clouds form and evolve over a range of spatial and temporal scales in response to a complex interaction of cloud microphysics with radiation, convection, and large-scale dynamics. This makes it especially challenging to interpret where and why clouds form and for climate models to represent them faithfully.

Tropical clouds, i.e. those found within approximately 23.5 degrees of the equator, appear in three distinct cloud populations or "modes": shallow cumulus, mid-level congestus and deep cumulonimbus (Johnson et al. 1999). A simple way to demonstrate the existence of the three modes is by inspection of the tropical-mean cloud fraction from CloudSat/CALIPSO observations (Figure 1a; Bertrand et al. 2024), which reveal three peaks in the vertical distribution of cloudiness. Shallow cumulus, also known as fair-weather clouds, form at the top of the boundary layer and cool the climate by reflecting sunlight (Cesana et al. 2019; Albrecht et al. 2019). Precipitating cumulonimbus rise out of the boundary layer and detrain near the tropopause, forming anvils as the cloudy air spreads out laterally (Hartmann
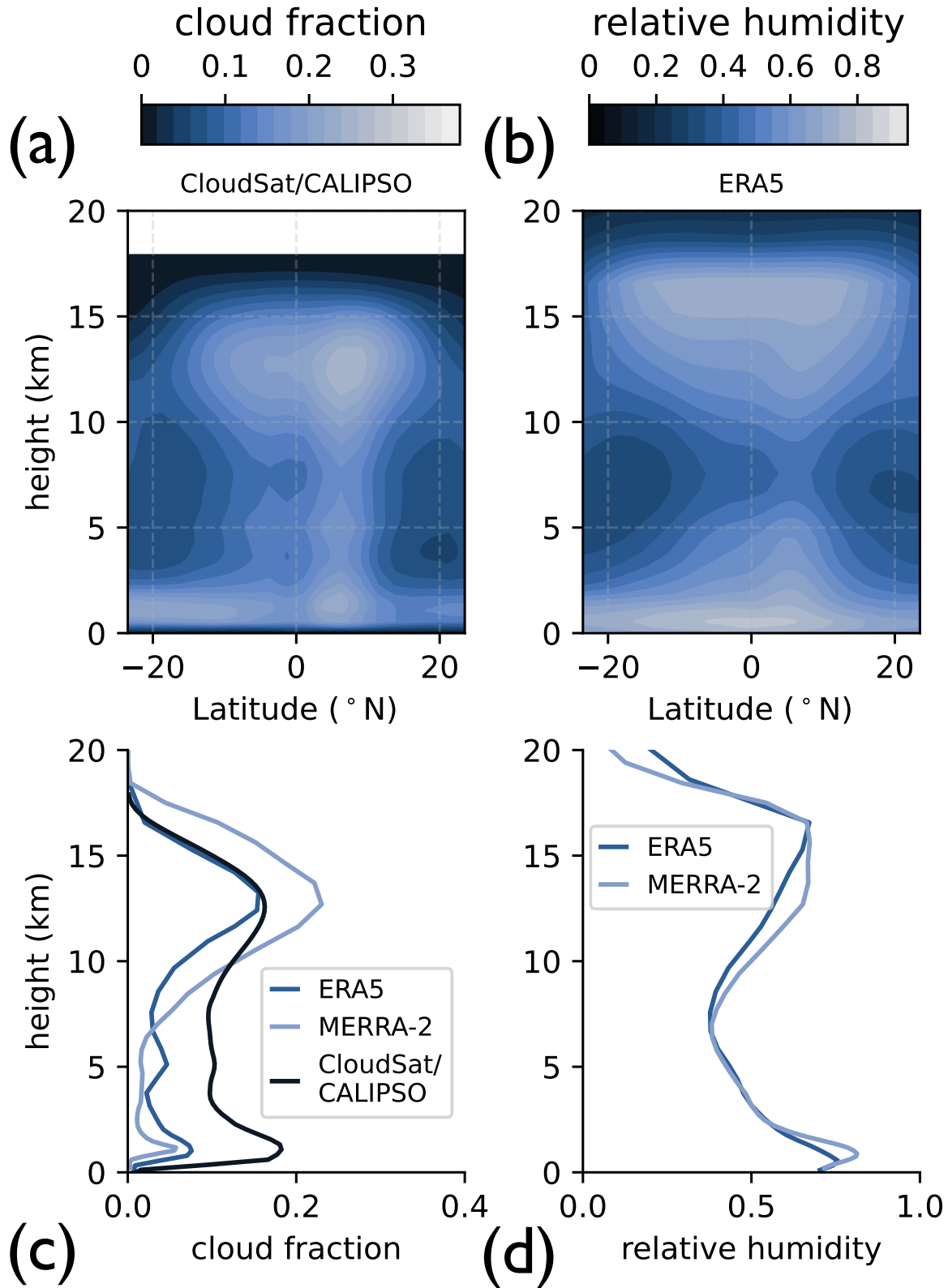
Corresponding author: Francisco E. Spaulding-Astudillo
fspauldinga@ucla.edu

Figure 1. (a) Zonal-mean average of cloud fraction from combined CloudSat/CALIPSO observations (Bertrand et al. 2024). (b) Zonal-mean average of relative humidity from the ERA5 reanalysis (Hersbach et al. 2023). Zonal- and meridionally-averaged (c) cloud fraction and (d) relative humidity from the ERA5 and MERRA-2 climate re-analyses (Global Modeling and Assimilation Office 2015). The temporal coverage is from 2006-2019, and the spatial coverage is all longitudes between 23.5°N/S.

et al. 2018; Romps 2014). The detraining anvils are also associated with the production of thin, high cirrus, which have a greenhouse warming effect on the climate (Sassen et al. 2009). Congestus clouds extend well above shallow cumulus but are less vertically developed than deep cumulonimbus, terminating in the mid-troposphere (Wall et al. 2013; Mechem & Oberthaler 2013). Thin, mid-level clouds with a cooling effect are ubiquitous in the tropics and are associated with convective detrainment at congestus peaks (Bourgeois et al. 2016).

Unlike the other modes, congestus cloud tops form where the horizontally-averaged relative humidity tends to be low (Figure 1d). From a purely microphysical perspective of cloud formation, this result is counter-intuitive because cloud droplets grow in air that is locally above saturation (Houze 2014), and observations and simulations affirm this relationship between cloudy areas and high relative humidity empirically (Figure 1a,b). Congestus clouds play an important role in humidifying the middle troposphere (Hohenegger & Stevens 2013) and are responsible for 25-40% of the total rainfall in the tropics (Johnson et al. 1999; Petty 1999). At the same time, global climate model simulations and reanalyses[1] are notoriously poor at representing the congestus mode. This can be seen by comparing CloudSat/CALIPSO observations (Bertrand et al. 2024) to the MERRA-2 (Gelaro et al. 2017) and ERA5 (Hersbach et al. 2020) reanalysis products (Figure 1c compares the horizontal averages of all three). In observations, the middle (congestus) mode is less pronounced than the low and high modes (Figure 1c). Reanalyses are global climate model simulations that incorporate real observations through data assimilation (Baatz et al. 2021). Figure 1 reveals the well-known problem (Miao et al. 2019; Bodas-Salcedo et al. 2008; Sokol & Hartmann 2022) that reanalyses (and climate model simulations in general) often underestimate the mid-level cloud fraction and/or lack the mid-tropospheric peak observed at ∼5 km in CloudSat/CALIPSO (Figure 1a,c). To the credit of ERA5, this reanalysis does display a congestus peak; many cloud-resolving models do not (Sokol & Hartmann 2022). A similar discrepancy between observations and reanalyses can be seen also in the representation of low clouds (Figure 1c). These persisting challenges reveal an opportunity to improve understanding of cloud formation in general. A goal of this paper is to investigate the origin of the mid-tropospheric (congestus) peak in tropical cloud fraction.

Tropical congestus clouds reach their peak altitude at 5-6 km, with the spread indicative of the typical values over ocean and land areas (Wall et al. 2013). Two theories based on buoyancy arguments have been proposed to explain the height of the congestus peak: the weak stability theory and the dry-air entrainment theory. The shared premise of these theories is that some process decelerates cloudy air as it ascends, causing it to accumulate and spread out preferentially at this level (Redelsperger et al. 2002; Jensen & Del Genio 2006). The weak stability theory posits that semi-permanent and/or transient stable layers in the mid-troposphere act as barriers to convective cloud development. Physically, the rising cloud registers the stable layer as negative buoyancy, forcing it to stall. The proposed mechanisms that promote weak stability invoke water phase changes, such as local evaporation of detrained cloud condensate (Nuijens & Emanuel 2018), sublimation cooling associated with dry air intrusions (Zuidema et al. 2006), and melting of stratiform cloud ice as it crosses the 0°C freezing level at 4-5 km in typical tropical conditions (Johnson et al. 1996). The freezing level is commonly referenced in studies of tropical congestus (Johnson et al. 1999; Jensen & Del Genio 2006; Mechem & Oberthaler 2013) because their tops are prevalent near it. The second theory, dry-air entrainment, asserts that congestus clouds peak in the mid-troposphere where the relative humidity is lowest due to buoyancy loss from mixing between the cloud and its dry environment (Brown & Zhang 1997). A strong consensus as to which mechanism is most important to congestus clouds seems to be lacking, with some arguing in favor of weak stability (Zuidema 1998; Riihimaki et al. 2012) or dry-air entrainment (Brown & Zhang 1997; Takemi et al. 2004; Jensen & Del Genio 2006; Takayabu et al. 2010; Kumar et al. 2014) or both (Johnson et al. 1999; Redelsperger et al. 2002). There is, on the other hand, concordance between observations and cloud-resolving model simulations that congestus clouds are more prevalent where the mid-level relative humidity is low (Brown & Zhang 1997; Redelsperger et al. 2002; Takemi et al. 2004; Jensen & Del Genio 2006; Kumar et al. 2014; Sokol & Hartmann 2022). These studies also find that areas with low mid-level relative humidity have fewer deep convective clouds (cumulonimbus).

A well-rounded theory of congestus cloud top formation should be able to explain (1) the 5-6 km peak in cloud fraction *and* (2) the enhancement of congestus by low mid-tropospheric relative humidity. While weak stability at, for instance, the freezing level of water may indicate why congestus clouds terminate near 5 km, it does not explain the invigoration of congestus clouds by low mid-tropospheric relative humidity. Similarly, the dry-air entrainment theory implies that congestus/cumulonimbus clouds should be more/less prevalent when the mid-level relative humidity is

---

[1] Global climate models simulate very large spatial domains and thus are distinct from cloud-resolving models, which are run over small domains at much higher resolution.

low, but it does not tell us why congestus clouds peak at 5-6 km, which is well below the tropospheric minimum in relative humidity at 7.5 km (Figure 1d). Of course, there may be a coordination between both buoyancy-reduction mechanisms that reproduce the observations. *Therefore, the aim of this study is to forge a new perspective of congestus cloud formation that accounts for a greater array of the observations.* Our hypothesis for the origin of congestus clouds and their invigoration builds on the so-called fixed anvil temperature (FAT) hypothesis, which we now describe.

Hartmann & Larson (2002) hypothesized a connection between the height of anvil clouds and the infrared emissivity of water vapor, which ultimately determines the ability of the atmosphere to radiatively cool. Notably, a reduction in emissivity around the 200 hPa level produces a swift decline in radiative cooling. This phenomenon is realized in cloud-resolving model simulations (Zelinka & Hartmann 2010), wherein the strongest convective outflow occurs precisely where radiative cooling declines at the fastest rate with increasing height. Given that the concentration of water vapor in the upper troposphere is primarily governed by temperature, it was hypothesized that these anvil clouds should consistently form at a specific temperature. The FAT hypothesis is generally backed by the results of observation and modeling (Kuang & Hartmann 2007; Zelinka & Hartmann 2010; Li et al. 2012). We note that a few studies have recently challenged the notion of a strictly fixed cloud-top temperature (Seeley et al. 2019a; Seidel & Yang 2022). The underlying cause of the decline in emissivity at the upper tropospheric boundary was later clarified by Jeevanjee & Fueglistaler (2020a). Employing a line-by-line radiative transfer model, they revealed that the diminishing upper-tropospheric emissivity in clear-sky regions partly stems from a decrease in the abundance of strongly-absorbing wavenumbers within the rotational band of water vapor above the 200 hPa level. Their result motivates the question: can the congestus peak be similarly understood through clear-sky infrared emissivity? In the annual mean, the tropical (and subtropical) area extending from 25°S to 25°N is approximately in a state of energy balance between radiative, latent, and sensible heating known as radiative-convective equilibrium (RCE; Jakob et al. 2019). Strictly speaking, the tropics (the area between ±23.5° latitude) are close to, but not quite in, RCE. In RCE scenarios where the contribution from latent heating dominates, moist convection organizes into fast, narrow updrafts and slow, widespread downdrafts (Bjerknes 1938; Singh & O'Neill 2022). It is reasonable to assume that most of this latent heating occurs in ascending cloudy regions. Since clouds are effective at limiting the outgoing longwave radiation to space, it is also reasonable to assume that most of the radiative cooling occurs in the descending clear-sky regions. Since cloudy regions and clear-sky regions are energetically connected, the physics that governs one must also influence the other. From this simple conceptual picture, a *clear-sky* mechanism of cloud formation emerges in which cloudy air converging into clear-sky regions is connected to vertical decreases in the clear-sky cooling rate. The "clear-sky convergence" (CSC) hypothesis is at the heart of the FAT hypothesis (Seeley et al. 2019b), and its applications could be broader than previously recognized. In this study, we test the CSC hypothesis against congestus clouds.

2. A CLEAR-SKY HYPOTHESIS OF CLOUD FORMATION IN RADIATIVE-CONVECTIVE EQUILIBRIUM

We now develop a predictive model of cloud-top formation based on the CSC hypothesis. Consider an idealized tropical environment in which there is widespread subsidence in clear-sky regions and narrow ascent in cloudy regions (Figure 2a), which are linked by mass balance (Hartmann & Larson 2002; Seeley et al. 2019a). We assume that anvil clouds are generated over large horizontal areas due to the convergence of cloud water into clear-sky regions, an assumption that is supported by cloud-resolving model simulations (Zelinka & Hartmann 2010; Beydoun et al. 2021; Jeevanjee & Zhou 2022). Conservation of energy for air parcels in clear-sky regions can be expressed as

$$c_p \rho \frac{DT}{Dt} - \frac{Dp}{Dt} = -H, \tag{1}$$
$$\quad (i) \qquad (ii) \qquad (iii)$$

where ρ $[kg/m^3]$ is density, c_p $[J/(kgK)]$ is the specific heat of environmental air at constant pressure, p $[Pa]$ is pressure, H $[J/(m^3 s)]$ is diabatic heating (by convention, positive values for cooling), and

$$\frac{D}{Dt} = \frac{\partial}{\partial t} + u\frac{\partial}{\partial x} + v\frac{\partial}{\partial y} + \omega\frac{\partial}{\partial p}, \tag{2}$$

is the total (Lagrangian, parcel-following) time derivative in pressure coordinates (Holton & Hakim 2013). In Equation 2, the horizontal derivatives are evaluated at constant pressure, u and v are horizontal velocities $[m\ s^{-1}]$ and ω is the pressure velocity $[Pa\ s^{-1}]$. Conservation requires the change in energy density of the air (i) and subsidence warming (ii) balance diabatic cooling (iii), the latter including both radiative and latent heating. The weak temperature gradients
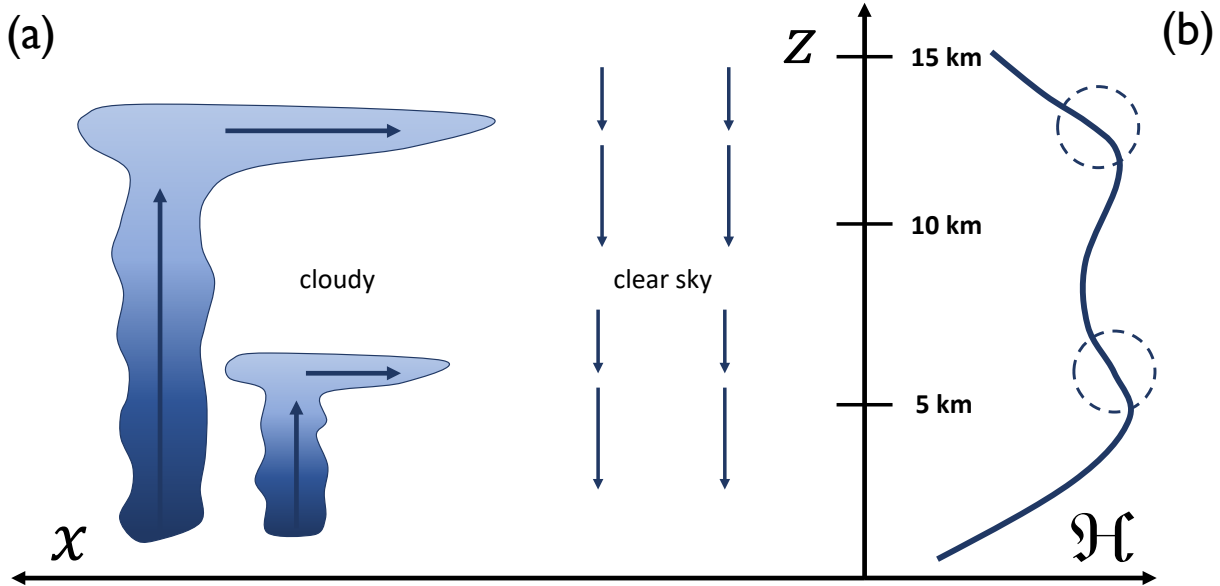
Figure 2. The radiative-convective perspective of cloud formation links the decline with altitude in clear-sky radiative cooling $\mathcal{H}$ to the net transport of cloudy air into clear-sky regions, as demanded by the vertical divergence of air in clear-sky regions. Schematically (b), there are two regions where $\mathcal{H}$ decreases with height, which are associated with middle and high peaks in cloud fraction (a). The high-altitude peak at ~ 12 km is associated with cumulonimbus anvils. Our study focuses on the middle "congestus" peak at ~ 6 km.

at low latitudes (Sobel et al. 2001) justify an additional assumption that temperature is horizontally homogeneous, allowing us to discard the horizontal thermal advection terms. In steady state (temperature and pressure not evolving in time), the energy budget simplifies to

$$\omega\Big(\frac{\partial T}{\partial p} - \frac{1}{c_p\rho}\Big) = -\frac{\mathrm{H}}{c_p\rho},$$

$$\omega\big(\Gamma_d - \Gamma\big) = \frac{\mathrm{H}}{c_p}g, \tag{3}$$

where in the first step we divided through by $c_p\rho$ and in the second step we invoked hydrostatic balance (multiplying through by $\partial_z p = -\rho g$ where g is the surface gravity and ∂_z is the vertical derivative) and used the definitions of the environmental lapse rate, $\Gamma = -\partial_z T$, and the dry adiabatic lapse rate, $\Gamma_d = g/c_p$. Next, we assume that the diabatic cooling in clear-sky regions is primarily radiative. This could be a poor assumption if, for example, there is also strong re-evaporation, which we here neglect. Jeevanjee & Zhou (2022) show that re-evaporation of cloud condensate is a potentially important source of local cooling that can increase the CSC. Under typical conditions, the net radiative heating is positive, indicating that the infrared cooling dominates. Though the contribution to net heating from shortwave absorption is likely to be non-negligible (Jeevanjee & Romps 2018), we choose to ignore it and approximate H by the infrared cooling rate $\mathcal{H}$ (positive for cooling). Using the definition of the deviation from static stability $\sigma = \Gamma_d - \Gamma$ (positive values are stable to dry convection), the clear-sky mass flux ($M_{clr} = \omega/g$; positive for descending motion) is

$$M_{clr} = \frac{\mathcal{H}}{c_p\sigma}. \tag{4}$$

Equation 4 indicates that radiative cooling in a stable clear-sky environment supports steady subsidence. If Γ and $\mathcal{H}$ were constant with height (the former implying constant σ), then M_{clr} would be constant also. However, if $\mathcal{H}$ decreases with height or σ increases with height, Equation 4 indicates a vertical divergence of mass from that layer. By mass continuity, (vertical) divergence in M_{clr} must be balanced by clear-sky (horizontal) convergence:

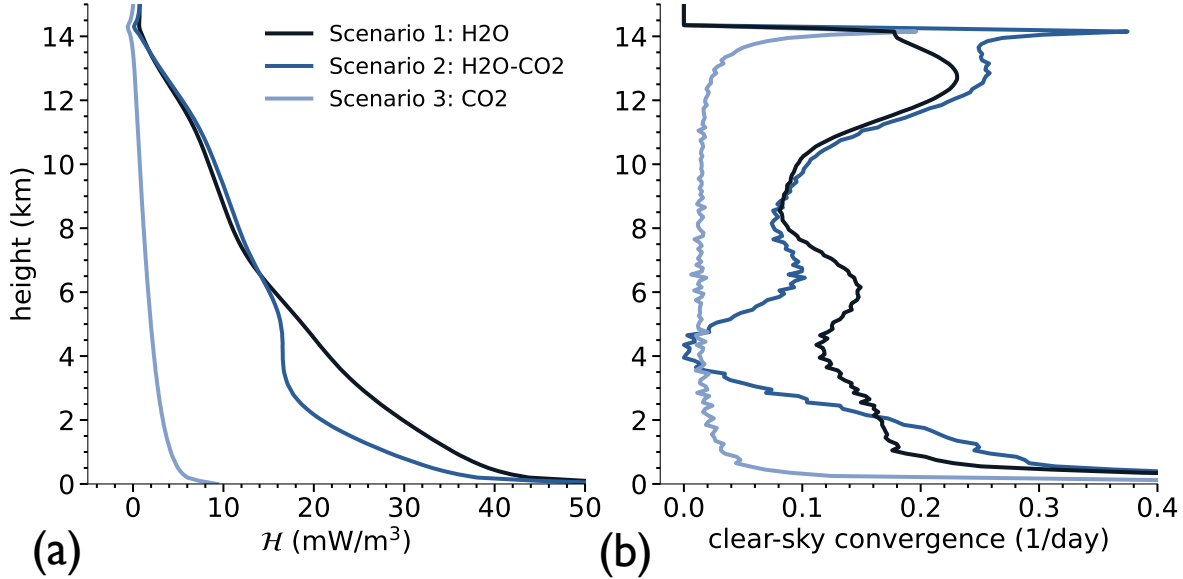$$\mathrm{CSC} = -\frac{1}{\rho}\frac{\partial M_{clr}}{\partial_z}$$

Figure 3. (a) Cooling rate $\mathcal{H}$ (Equation 7) from line-by-line computations with RFM and (b) clear-sky convergence (Equation 6) in three greenhouse gas scenarios.

$$= \frac{-1}{c_p\rho\sigma}\partial_z\mathcal{H} + \frac{\mathcal{H}}{c_p\rho\sigma^2}\partial_z\sigma. \tag{5}$$

Positive values of CSC support a net transport of air from the cloud into clear-sky regions – i.e., net detrainment – and following Seeley et al. (2019b) is specified with the units of an inverse timescale. *Equation 5 shows that CSC is supported either by a decrease in radiative cooling or an increase in stability with height.* In regions where the first term is positive, however, the second term is typically negative and thus reduces the net positive CSC (Seeley et al. 2019a). For now, we assume that the mid-tropospheric lapse rate is constant, and therefore that the CSC at the congestus level is dominated by vertical changes in the clear-sky cooling rate. In doing so, we could be eliminating a key possible reason for strong mid-tropospheric CSC: the presence of stable layers near the water freezing level. While we acknowledge this as a possibility, our reason to deliberately focus on the radiative cooling will soon become clear.

$$\text{CSC} \approx \max\left(0, \frac{-1}{c_p\rho\sigma}\partial_z\mathcal{H}\right). \tag{6}$$

Equation 6 is an expression of the CSC hypothesis, and this form will be assumed henceforth. The schematic in Figure 2 demonstrates the significance of this simple picture of cloud formation. Consider a hypothetical profile of clear-sky radiative cooling where the cooling rate decreases with height at two levels, $\partial_z\mathcal{H} < 0$ (Figure 2b), implying CSC at both levels (Figure 2a; Equation 6). Clouds must detrain at these heights to supply the mass demanded by the vertical divergence of clear air, implying that anvil clouds increase the areal cloud fraction. Tall, cumulonimbus towers with spreading anvils are thought to form by this mechanism, as depicted schematically in Figure 2a. We hypothesize that this same picture applies to congestus clouds and, if so, a decrease in clear-sky cooling must preferentially occur between 5-6 km by the action of one or more of Earth's greenhouse gases.

3. CONGESTUS CLOUDS ARE ASSOCIATED WITH SPECTRAL FEATURES OF WATER VAPOR

Using the cooling profiles from the H2O, H2O-CO2, and CO2 scenarios (see Methods), we solve for the CSC using Equation 6 (Figure 3b). Below the tropopause, $\mathcal{H}$ monotonically decreases with height in all scenarios (Figure 3a). By comparing scenarios with and without water vapor, we see the well-known fact that water vapor accounts for the overwhelming majority of tropospheric cooling (Figure 3a; Held & Soden 2000). Figure 3b demonstrates that regions where $\mathcal{H}$ falls off fastest with height give rise to the peaks in CSC, in accordance with Equation 6. Importantly, the cooling rate in scenarios that include water vapor have a strong local decrease in the mid-troposphere that produces a peak in CSC at 6 km. The scenario without carbon dioxide does not have CSC in the mid-troposphere, indicating

that the radiative properties of carbon dioxide do not contribute to CSC at these levels. H2O-CO2 demonstrates that the strong peak in mid-tropospheric CSC is not disrupted by the non-linear overlap of water vapor and carbon dioxide absorption lines. *Our line-by-line calculations reveal the possibility of a radiative origin for observed tropical congestus cloud tops* (Figure 1a).

To better understand the role of water vapor in driving CSC at 6 km, we resolve the spectral dimension of the cooling rate, $\mathcal{H}$ [Wm^{-3}]. $\mathcal{H}$ is, in fact, an integral over the spectrally-resolved cooling rate ($\tilde{\mathcal{H}}$; Wm^{-3}cm) in wavenumber space:

$$\mathcal{H}(z) = \int \tilde{\mathcal{H}}(\nu, z) d\nu \tag{7}$$

where ν is wavenumber [cm^{-1}] and z is height. We use tildes to identify any variable that is spectrally-resolved: i.e., a function of wavenumber. For now, we leave Equation 7 as an indefinite integral, and comment on the bounds of integration later. When we say colloquially that an atmospheric layer is radiatively cooling, we mean that more radiation is going out than coming in. In the case of a molecule like water vapor in Earth's tropics, it is reasonable to make the cooling-to-space (CTS) approximation (Jeevanjee & Fueglistaler 2020b). In the CTS approximation, we assume that the non-local upwelling and downwelling fluxes cancel out, and so the net upward flux at any given height is equal to the fraction of the local blackbody emission that escapes to space (Jeevanjee & Fueglistaler 2020a).[2] We define the ratio of the emitted radiation-to-space to the blackbody radiation as the "emissivity-to-space" (Jeevanjee & Fueglistaler 2020a) and represent it symbolically as $\tilde{\epsilon}$. The CTS approximation isn't necessary for our arguments, but it brings to the fore the underlying mechanism for CSC in Earth's middle troposphere. The cooling rate in the CTS approximation may be expressed as a spectral integral over the product of two terms

$$\mathcal{H}_{cts}(z) = \int \pi\tilde{B} \times \partial_z\tilde{\epsilon} \, d\nu \tag{8}$$

$$(i) \qquad (ii)$$

where $\tilde{B}(\nu, T)$ is the Planck function for blackbody radiation. The terms in Equation 8 can be understood as follows: (i) $\pi\tilde{B}(\nu, T)$ is the blackbody emission at the local temperature T [Wm^{-2}cm] [3] and (ii) $\partial_z\tilde{\epsilon}$ is the emissivity-to-space gradient [m^{-1}]. $\tilde{\epsilon}$ is only a function of the optical depth,

$$\tilde{\tau} = \int_0^p \tilde{\kappa}(\nu, p, T) \, q \, dp/g, \tag{9}$$

which is, by convention, zero at the top of the atmosphere and increases monotonically towards the surface (Jeevanjee & Fueglistaler 2020b); and, in turn, depends almost entirely on pressure p, specific humidity q, and the absorption lines of water vapor $\tilde{\kappa}$. Since relative humidity is uniform and the lapse rate is constant in our "H2O" scenario, a swift decline (curvature) in the cooling rate can only emerge through $\tilde{\kappa}$.

Consider the absorption lines of water vapor at a reference temperature and pressure of 260 K and 500 hPa (Figure 4c), $\tilde{\kappa} = \tilde{\kappa}_{ref}(\nu, 500\text{hPa}, 260\text{K})$; absorption per unit mass is larger in the peaks than in the valleys. Figure 4a shows $\tilde{\mathcal{H}}_{cts}$ in H2O. It is clear that most of the cooling originates from the water vapor rotation band.[4] Examining the tropospheric blackbody emission (Figure 4b) helps elucidate this phenomenon. The Earth's tropospheric temperature range situates the emission peak roughly between 400-600 cm^{-1}, aligning the maximum values of $\pi\tilde{B}$ (those exceeding 0.3 Wm^{-2}cm) with the water vapor rotation band. The non-uniform abundance of absorption lines in this band is the primary factor contributing to the strong curvature in the cooling rate. To substantiate this claim, we present 1D and 2D histograms depicting the spectral density of absorption lines (Figure 4d). Two distinct regions exhibit a significant drop in the line density. The first region, located near 40 m^2/kg (Jeevanjee & Fueglistaler 2020a), coincides with the upper-tropospheric peak in CSC associated with cumulonimbus anvils. The second region, spanning 0.3-1.1 m^2/kg, is associated with strong cooling between 5.2-6.9 km, as detailed in Appendix A. The absorption lines in Figure 4c represent distinct transitions in the quantum state of water vapor molecules (Pierrehumbert 2010). We do not possess a quantum mechanical explanation for this intruiging drop in rotational line abundance, but it is natural to wonder whether one exists. Pursuing such understanding is a task for future work. The spectral features of water vapor thus provide a firm constraint on the mid-tropospheric CSC and, potentially, the location of congestus cloud tops.

---

[2] In Appendix B, we verify that the CTS approximation agrees to within ~10% with $\mathcal{H}$ for water vapor and, more importantly, $\mathcal{H}_{cts}$ decreases rapidly with increasing height between 5-6 km.

[3] The pre-factor of π comes from an integral of the spectral intensity over all upper-hemispheric solid angles (e.g., see Rybicki & Lightman 1985)

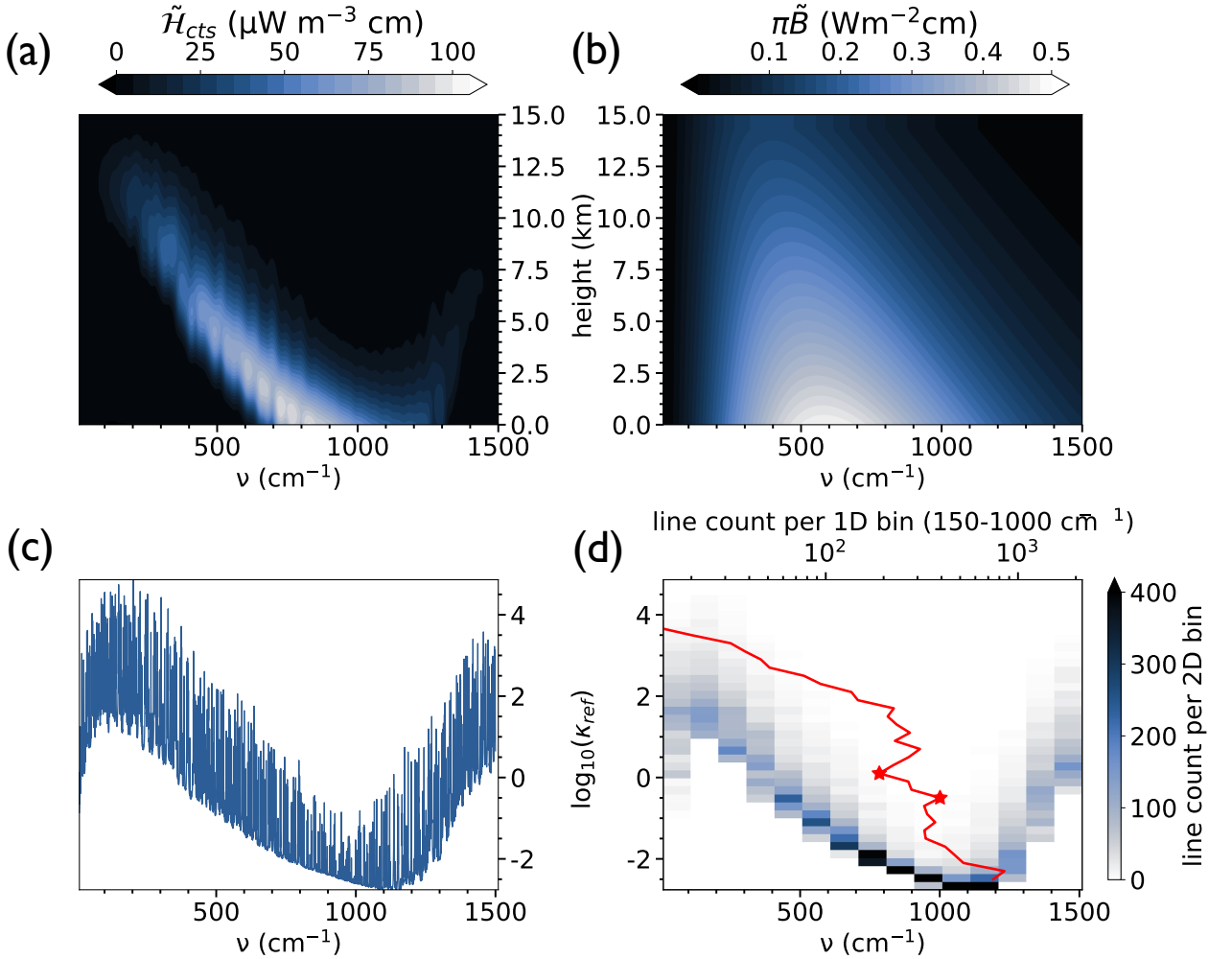[4] The rotation band is the spectral region to the left of ~1000 cm^{-1}.

Figure 4. (a) Radiative cooling rate under the cooling-to-space approximation $\tilde{\mathcal{H}}_{cts}$ (Equation 8) and (b) tropospheric blackbody emission $\pi\tilde{B}$. Both are resolved in wavenumber and height and vertically smoothed with a Gaussian filter. (c) Logarithm of the reference absorption coefficient of water vapor $\tilde{\kappa}_{ref}$ at 500 hPa and 260 K. (d) Two-dimensional (2D) histogram of absorption line abundance in 100 cm^{-1} and 0.2 wavenumber-log$_{10}(\tilde{\kappa}_{ref})$ bins. The red line is a one-dimensional (1D) histogram of absorption line abundance over a single spectral bin between 150-1000 cm^{-1} in 0.2 increments of log$_{10}(\tilde{\kappa}_{ref})$. Red stars mark a sharp drop in rotation-band line abundance between 0.3-1.1 m^2/kg.

4. CONGESTUS INVIGORATION BY LOW RELATIVE HUMIDITY IN THE MID-TROPOSPHERE

A confounding property of spreading congestus cloud tops is that they occur in areas of low horizontally-averaged relative humidity (Figure 1), which is characteristic of the tropical mid troposphere. In fact, observations and cloud-resolving model simulations indicate that more mid-level clouds and fewer upper-level clouds occur in regions of relatively lower mid-tropospheric humidity (Redelsperger et al. 2002; Takemi et al. 2004; Kumar et al. 2014; Sokol & Hartmann 2022). Near the surface in the planetary boundary layer, evaporation from the tropical oceans pins the relative humidity to values near saturation. The vertical distribution of relative humidity in the tropical atmosphere above the boundary layer is the result of a competition between subsidence drying and convective moistening (Romps 2014). The dominant mechanism switches from subsidence drying to convective moistening around 7.5 km, producing the characteristic "C-shape" in tropical relative humidity (Figure 1e). In the previous section, we showed that water vapor spectral features constrain the height of strong mid-tropospheric CSC and potentially also congestus cloud tops – recall that we arrived at this result using RFM in an idealized setup with a constant lapse rate and uniform relative humidity.
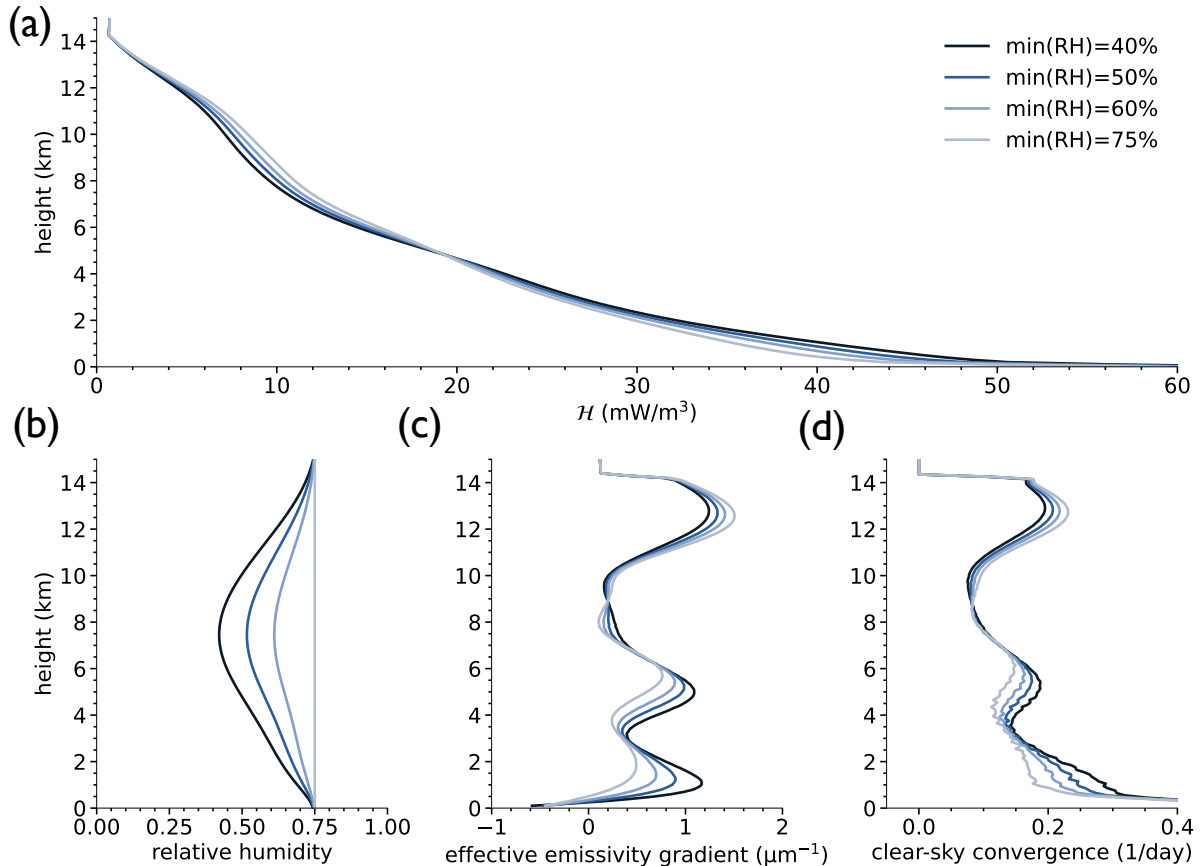
Figure 5. (a) Cooling rate $\mathcal{H}$ (Equation 7) from line-by-line computations with RFM in scenarios of varying (b) relative humidity. (c) Vertical gradient of effective emissivity (Equation 10) and (d) clear-sky convergence (Equation 6). The data are from H2O and H2O-C.

Under the conventional view, a decline in emissivity with height is required for anvil cloud formation (e.g., Hartmann & Larson 2002). We define an effective emissivity-to-space ϵ such that its vertical gradient is

$$\partial_z \epsilon(z) = \frac{\int_{150cm^{-1}}^{1000cm^{-1}} \pi \tilde{B} \times \partial_z \tilde{\epsilon} \, d\nu}{\int_{150cm^{-1}}^{1000cm^{-1}} \pi \tilde{B} \, d\nu}. \tag{10}$$

These terms should look familiar, as they also appear in Equation 8. The conventional view finds validation in Figure 5c where we see that the middle and upper layers of convective outflow coincide with the largest gradients in ϵ. In typical conditions where temperature decreases with height, a strong emissivity gradient tells us to expect strong CSC. It is tempting to think that the mechanism that sets the height of congestus cloud tops is the same as that for the highest clouds anvils. This may be the case, but such a conclusion cannot be reached solely on the basis of the CSC hypothesis. Our simplified formalism of the CSC hypothesis (Equation 6) indicates detrainment at certain heights if mass and energy are conserved, but the same formalism does not tell us what forces are responsible for the inhibiting the vertical growth of the clouds. Though radiation might play an important role, the detrainment implied by the CSC hypothesis is not necessarily radiatively-driven. The limitations of the CSC hypothesis are discussed further in Section 5. The existence of stable layers in the vicinity of congestus cloud tops is another complication. Whereas the highest cloud anvils detrain far from stable layers (e.g., the tropopause; Seeley et al. 2019b), congestus clouds frequently terminate near stable layers produced by water phase changes (Johnson et al. 1996; Nuijens & Emanuel 2018; Zuidema et al. 2006). Our simplified formalism neglects vertical deviations in stability, but, in reality, such deviations impact the total CSC (Equation 5). Weighing the competing influences at congestus cloud tops is a task for future work.

Having argued for the existence of a radiative influence on congestus cloud tops, we next explore the effect of the "C-shape" in the vertical profile of relative humidity (Figure 5b) on the congestus mode. Figure 5d demonstrates that reducing the mid-level relative humidity locally enhances the CSC at middle levels and also reduces CSC at upper levels relative to the scenario with uniform relative humidity. Decreasing the relative humidity in this manner has two distinct radiative effects. First, it reduces the number of water vapor molecules at every level. This, in turn, forces the mid-level peak in CSC to descend from 6.0 km at 75% constant relative humidity to 5.3 km at 40% mid-tropospheric relative humidity (Figure 5d).[5] The downward shift is explained by the fact that a drier troposphere increases the path length between the top of the atmosphere and the $\tilde{\tau} \approx 1$ levels in the water vapor rotation band, which determine where the strong gradients in radiative cooling, $\partial_z \mathcal{H}$, occur. Second, reducing the mid-tropospheric relative humidity accelerates the declining abundance of water molecules below 7.5 km, which increases the emissivity-to-space gradient (Figure 5c). This translates into a larger $\partial_z \mathcal{H}$ that in turn enhances the CSC in this region (Equation 6). In summary, a drier mid-troposphere promotes stronger CSC and this should lead to an enhancement of the mid-level clouds.

Our spectral interpretation of congestus enhancement is consistent with the invigoration of the congestus mode in cloud-resolving simulations in which convective aggregation emerges (Sokol & Hartmann 2022). The two consequences of aggregation that lead to congestus invigoration in their study are (1) a decrease in the mid- and upper-level relative humidity and (2) a stronger decrease in radiative cooling across the congestus level, which Sokol & Hartmann (2022) collectively refer to as the "radiative-divergence feedback". Our line-by-line experiments with RFM bring additional clarity to the origin of this feedback. Congestus invigoration stems from two fundamental sources: (1) a drop in the spectral density of absorption lines in the water vapor rotation band that gives rise to a peak in CSC around 5-6 km and (2) a mid-level reduction in relative humidity that hastens the decline in $\mathcal{H}$ across the congestus level. Sokol & Hartmann (2022) find convective aggregation enhances the latter.

5. DISCUSSION

The processes that control the height and abundance of congestus clouds have been debated for decades. The debate has centered on the dry-air entrainment and the weak stability theories. In observational and modeling studies, these theories have been used successfully to show that the ascent of convective clouds can be arrested by buoyancy loss via entrainment and/or the presence of stable layers near the freezing level. These preceding theories individually fall short in offering a comprehensive explanation for two phenomena: first, that congestus clouds peak at 5-6 km and, second, that they are invigorated by low mid-tropospheric relative humidity. Therefore, the aim of this study has been to forge a complementary perspective of cloud formation that can explain a greater array of the observations.

The central result of this work is that a drop in the spectral density of absorption lines within the water vapor rotation band is the cause of a local, rapid decrease in the clear-sky cooling rate that, in turn, produces a peak in clear-sky convergence (CSC) between 5-6 km, a region associated with congestus cloud-top formation in the tropics (Wall et al. 2013). An equivalent statement is that congestus cloud tops form near to strong clear-sky gradients in the water vapor emissivity. We also demonstrated that a drier mid-troposphere creates larger gradients in water vapor emissivity that, in turn, enhance CSC. This implies more convective outflow at middle levels and less at upper levels, consistent with the observations. The CSC hypothesis is derived from the basic building blocks of mass and energy conservation in radiative-convective equilibrium, which is approximately satisfied in the spatio-temporal mean of ~ 1 year over an area of ~ 5000 km centered on the equator (i.e., $\pm 25°$ latitude; Jakob et al. 2019). It provides a firm constraint on the net detrainment of cloudy air at specific heights of the atmosphere. There are, however, competing influences with radiation on CSC that we neglected. We chose to focus on the influence of radiation in order to highlight the clear-sky water vapor absorption feature, but stable layers near the freezing level of water vapor and re-evaporation of detrained cloud condensate can modify the CSC as well (e.g., Jeevanjee & Zhou 2022). The relative importance of these processes in the mid-troposphere merits further study. Our conclusions are based on theoretical considerations and results obtained from a line-by-line radiative transfer model.

The buoyancy-based theories and the CSC hypothesis offer complementary insights into cloud top formation, but each have an important set of limitations. The CSC hypothesis indicates where clouds must strongly detrain, but not why. It cannot explain the forces behind the response, nor their relative influence. Clouds detrain as a response to external forces, with the height of each cloud directly determined by its buoyancy (Takahashi & Luo 2012). The buoyancy-based theories are possible explanations for why individual cloud development is restricted. Until recently

---

[5] 40% relative humidity in the mid-troposphere and a congestus peak of 5.3 km is more consistent with tropical reanalyses and observations (Figures 1c,d).

(e.g., Sokol & Hartmann 2022), the potential influence of radiative processes on restricting congestus cloud tops to 5-6 km and enhancing their formation in dry conditions has been overlooked. Radiative processes impact the vertical temperature structure and thus the buoyancy of congestus clouds. The existence of a clear-sky water vapor absorption feature in the mid-troposphere suggests that radiative processes could systematically influence buoyancy in this region, a possibility that is revealed through the CSC hypothesis. The relative influence of radiation, stability, and entrainment on buoyancy should be assessed in future work, and this could lead to a consensus about the physical origin of congestus clouds.

6. METHODS

We employ the Reference Forward Model (RFM; Dudhia 2017) for line-by-line radiative transfer calculations at high resolution over a clear column of atmosphere. We use a vertical resolution of 100 m between the surface and the top of atmosphere at 30 km and a spectral resolution of 0.1 cm^{-1} between 10-1500 cm^{-1}. This spectral range was chosen because it includes 93% of the spectrally-integrated emission from a 300 K blackbody and 99% of the spectrally-integrated emission from a 200 K blackbody, the characteristic range of temperatures in the tropics. In our RFM calculations, we use the most recent line absorption data from the 2020 High-Resolution Transmission (HITRAN; Gordon et al. 2022) release. Continuum absorption by water vapor and carbon dioxide are included (where applicable) in our calculations, which are represented in RFM according to Mlawer et al. (2012) and Edwards (1992). Since oxygen and nitrogen are transparent to infrared radiation, we do not include them in our line-by-line calculations. As model inputs, we provide vertically-resolved profiles of temperature, pressure, and absorber mixing ratio that are representative of the tropical atmosphere. These inputs include a surface pressure and temperature of 1 bar and 300 K, a uniform lapse rate of 7 K/km,[6] and an isothermal stratosphere of 200 K. From these inputs, RFM computes the clear-sky infrared cooling rate, optical depth, transmissivity, and molecular absorption coefficients as a function of height, temperature, absorber concentration, and wavenumber. The line-by-line cooling rates from RFM are used to calculate the clear-sky convergence (Equation 6)

We construct four greenhouse gas scenarios for line-by-line radiative transfer calculations with RFM: (1) H2O: Water vapor is the only absorber in this scenario. The troposphere has a uniform relative humidity of 75% and the stratospheric water vapor molar mixing ratio is pegged to the tropopause value; (2) H2O-CO2: This scenario includes carbon dioxide as well as water vapor as absorbing species. The molar mixing ratio of carbon dioxide is set to 350 ppmv at every height. Again, the relative humidity with respect to water vapor is 75% in the troposphere and, in the stratosphere, the water vapor molar mixing ratio is fixed to the tropopause value; (3) CO2: Carbon dioxide is the sole absorber with a uniform mixing ratio of 350 ppmv; (4) H2O-C: Water vapor is the only absorber. Relative humidity is allowed to vary with height. The shape of the profile is described in the main text. The stratosphere has a water vapor molar mixing ratio fixed at the tropopause value.

The data and code from this study is freely available at 10.5281/zenodo.10139065.

---

[6] This is a simplifying assumption of constant deviation from static stability, σ (Equation 6). Note that σ decreases with height in typical conditions, which reduces the total CSC.

REFERENCES

Albrecht, B., Ghate, V., Mohrmann, J., et al. 2019, Bulletin of the American Meteorological Society, 100, 93, doi: 10.1175/BAMS-D-17-0180.1

Baatz, R., Hendricks Franssen, H. J., Euskirchen, E., et al. 2021, Reviews of Geophysics, 59, e2020RG000715, doi: https://doi.org/10.1029/2020RG000715

Bertrand, L., Kay, J. E., Haynes, J., & de Boer, G. 2024, Earth System Science Data, 16, 1301, doi: 10.5194/essd-16-1301-2024

Beydoun, H., Caldwell, P. M., Hannah, W. M., & Donahue, A. S. 2021, Geophysical Research Letters, 48, e2021GL094049, doi: https://doi.org/10.1029/2021GL094049

Bjerknes, J. 1938, Q.J.R. Meteorol. Soc., 64, 325

Bodas-Salcedo, A., Webb, M. J., Brooks, M. E., et al. 2008, Journal of Geophysical Research: Atmospheres, 113, doi: https://doi.org/10.1029/2007JD009620

Bourgeois, Q., Ekman, A. M. L., Igel, M. R., & Ringer, M. A. 2016, Nature Communications, 7, doi: https://doi.org/10.1038/ncomms12432

Brown, R. G., & Zhang, C. 1997, Journal of the Atmospheric Sciences, 54, 2760 , doi: https://doi.org/10.1175/1520-0469(1997)054⟨2760: VOMMAI⟩2.0.CO;2

Ceppi, P., & Nowack, P. 2021, Proceedings of the National Academy of Sciences, 118, e2026290118, doi: 10.1073/pnas.2026290118

Cesana, G., Del Genio, A. D., & Chepfer, H. 2019, Earth System Science Data, 11, 1745, doi: 10.5194/essd-11-1745-2019

Crameri, F. 2023, Scientific colour maps, Zenodo, doi: 10.5281/zenodo.1243862

Dudhia, A. 2017, Journal of Quantitative Spectroscopy and Radiative Transfer, 186, 243, doi: https://doi.org/10.1016/j.jqsrt.2016.06.018

Edwards, D. P. 1992, University Corporation for Atmospheric Research, (No. NCAR/TN-367+STR), doi: 10.5065/D6W37T86

Gelaro, R., McCarty, W., Suárez, M. J., et al. 2017, Journal of Climate, 30, 5419 , doi: https://doi.org/10.1175/JCLI-D-16-0758.1

Global Modeling and Assimilation Office. 2015, MERRA-2 tavg3_3d_asm_Nv: 3d,3-Hourly,Time-Averaged,Model-Level,Assimilation,Assimilated Meteorological Fields V5.12.4, Greenbelt, MD, USA, Goddard Earth Sciences Data and Information Services Center (GES DISC), doi: 10.5067/SUOQESM06LPK

Gordon, I., Rothman, L., Hargreaves, R., et al. 2022, Journal of Quantitative Spectroscopy and Radiative Transfer, 277, 107949, doi: https://doi.org/10.1016/j.jqsrt.2021.107949

Hartmann, D. L., Dygert, B. D., Blossey, P. N., Fu, Q., & Sokol, A. B. 2022, Journal of Climate, 35, 6253 , doi: https://doi.org/10.1175/JCLI-D-21-0861.1

Hartmann, D. L., Gasparini, B., Berry, S. E., & Blossey, P. N. 2018, Journal of Advances in Modeling Earth Systems, 10, 3012, doi: https://doi.org/10.1029/2018MS001484

Hartmann, D. L., & Larson, K. 2002, Geophysical Research Letters, 29, 12, doi: 10.1029/2002GL015835

Held, I. M., & Soden, B. J. 2000, Annual Review of Energy and the Environment, 25, 441, doi: 10.1146/annurev.energy.25.1.441

Hersbach, H., Bell, B., Berrisford, P., et al. 2020, Quarterly Journal of the Royal Meteorological Society, 146, 1999, doi: https://doi.org/10.1002/qj.3803

—. 2023, ERA5 monthly averaged data on single levels from 1940 to present, Copernicus Climate Change Service (C3S) Climate Data Store (CDS), doi: 10.24381/cds.f17050d7

Hohenegger, C., & Stevens, B. 2013, Journal of the Atmospheric Sciences, 70, 448 , doi: https://doi.org/10.1175/JAS-D-12-089.1

Holton, J. R., & Hakim, G. J. 2013, in An Introduction to Dynamic Meteorology (Fifth Edition), fifth edition edn., ed. J. R. Holton & G. J. Hakim (Boston: Academic Press), 67–93, doi: https://doi.org/10.1016/B978-0-12-384866-6.00003-9

Houze, R. A. 2014, in International Geophysics, Vol. 104, Cloud Dynamics, ed. R. A. Houze (Academic Press), 47–76, doi: https://doi.org/10.1016/B978-0-12-374266-7.00003-2

Jakob, C., Singh, M. S., & Jungandreas, L. 2019, Journal of Geophysical Research: Atmospheres, 124, 5418, doi: https://doi.org/10.1029/2018JD030092

Jeevanjee, N., & Fueglistaler, S. 2020a, Journal of the Atmospheric Sciences, 77, 479 , doi: https://doi.org/10.1175/JAS-D-18-0347.1

—. 2020b, Journal of the Atmospheric Sciences, 77, 465 , doi: https://doi.org/10.1175/JAS-D-18-0352.1

Jeevanjee, N., & Romps, D. M. 2018, Proceedings of the National Academy of Sciences of the United States of America, 115, 11465, doi: 10.1073/pnas.1720683115

Jeevanjee, N., & Zhou, L. 2022, Journal of Advances in Modeling Earth Systems, 14, e2021MS002759, doi: https://doi.org/10.1029/2021MS002759

Jensen, M. P., & Del Genio, A. D. 2006, Journal of Climate, 19, 2105 , doi: https://doi.org/10.1175/JCLI3722.1

Johnson, R. H., Ciesielski, P. E., & Hart, K. A. 1996, Journal of Atmospheric Sciences, 53, 1838 , doi: https://doi.org/10.1175/1520-0469(1996)053⟨1838: TINTL⟩2.0.CO;2

Johnson, R. H., Rickenbach, T. M., Rutledge, S. A., Ciesielski, P. E., & Schubert, W. H. 1999, Journal of Climate, 12, 2397 , doi: https://doi.org/10.1175/1520-0442(1999)012⟨2397: TCOTC⟩2.0.CO;2

Kuang, Z., & Hartmann, D. L. 2007, Journal of Climate, 20, 2051 , doi: https://doi.org/10.1175/JCLI4124.1

Kumar, V. V., Protat, A., Jakob, C., & May, P. T. 2014, Journal of the Atmospheric Sciences, 71, 1105 , doi: https://doi.org/10.1175/JAS-D-13-0231.1

Li, Y., Yang, P., North, G. R., & Dessler, A. 2012, Journal of the Atmospheric Sciences, 69, 2317 , doi: https://doi.org/10.1175/JAS-D-11-0158.1

Mechem, D. B., & Oberthaler, A. J. 2013, Journal of Advances in Modeling Earth Systems, 5, 623, doi: https://doi.org/10.1002/jame.20043

Miao, H., Wang, X., Liu, Y., & Wu, G. 2019, Atmospheric Science Letters, 20, e906, doi: https://doi.org/10.1002/asl.906

Mlawer, E. J., Payne, V. H., Payne, V. H., et al. 2012, Philos Trans A Math Phys Eng Sci, 370, 2520, doi: 10.1098/rsta.2011.0295

Nuijens, L., & Emanuel, K. 2018, Quarterly Journal of the Royal Meteorological Society, 144, 2676, doi: https://doi.org/10.1002/qj.3385

Petty, G. W. 1999, Journal of Climate, 12, 220 , doi: https://doi.org/10.1175/1520-0442(1999)012⟨0220: POPFWT⟩2.0.CO;2

Pierrehumbert, R. T. 2010, Principles of Planetary Climate (Cambridge University Press), doi: 10.1017/CBO9780511780783

Redelsperger, J.-L., Parsons, D. B., & Guichard, F. 2002, Journal of the Atmospheric Sciences, 59, 2438 , doi: https://doi.org/10.1175/1520-0469(2002)059⟨2438: RPAFLC⟩2.0.CO;2

Riihimaki, L. D., McFarlane, S. A., & Comstock, J. M. 2012, Journal of Climate, 25, 6835 , doi: https://doi.org/10.1175/JCLI-D-11-00599.1

Romps, D. M. 2014, Journal of Climate, 27, 7432, doi: 10.1175/JCLI-D-14-00255.1

Rybicki, G. B., & Lightman, A. P. 1985, FUNDAMENTALS OF RADIATIVE TRANSFER (John Wiley & Sons, Ltd), 1–50, doi: https://doi.org/10.1002/9783527618170.ch1

Sassen, K., Wang, Z., & Liu, D. 2009, Journal of Geophysical Research: Atmospheres, 114, doi: https://doi.org/10.1029/2009JD011916

Seeley, J. T., Jeevanjee, N., Langhans, W., & Romps, D. M. 2019a, Geophysical Research Letters, 46, 492, doi: https://doi.org/10.1029/2018GL080747

Seeley, J. T., Jeevanjee, N., & Romps, D. M. 2019b, Geophysical Research Letters, 46, 1842, doi: https://doi.org/10.1029/2018GL080096

Seidel, S. D., & Yang, D. 2022, Journal of Climate, 35, 8065 , doi: https://doi.org/10.1175/JCLI-D-21-0962.1

Sherwood, S. C., Webb, M. J., Annan, J. D., et al. 2020, Reviews of Geophysics, 58, e2019RG000678, doi: https://doi.org/10.1029/2019RG000678

Singh, M. S., & O'Neill, M. E. 2022, Rev. Mod. Phys., 94, 015001, doi: 10.1103/RevModPhys.94.015001

Sobel, A. H., Nilsson, J., & Polvani, L. M. 2001, Journal of the Atmospheric Sciences, 58, 3650 , doi: 10.1175/1520-0469(2001)058⟨3650: TWTGAA⟩2.0.CO;2

Sokol, A. B., & Hartmann, D. L. 2022, Journal of Advances in Modeling Earth Systems, 14, e2022MS003045, doi: https://doi.org/10.1029/2022MS003045

Takahashi, H., & Luo, Z. 2012, Geophysical Research Letters, 39, doi: https://doi.org/10.1029/2012GL052638

Takayabu, Y. N., Shige, S., Tao, W.-K., & Hirota, N. 2010, Journal of Climate, 23, 2030 , doi: https://doi.org/10.1175/2009JCLI3110.1

Takemi, T., Hirayama, O., & Liu, C. 2004, Geophysical Research Letters, 31, doi: https://doi.org/10.1029/2004GL020225

Wall, C., Liu, C., & Zipser, E. 2013, Journal of Geophysical Research: Atmospheres, 118, 6478, doi: https://doi.org/10.1002/jgrd.50455

Zelinka, M. D., & Hartmann, D. L. 2010, Journal of Geophysical Research: Atmospheres, 115, doi: https://doi.org/10.1029/2010JD013817

Zuidema, P. 1998, Journal of the Atmospheric Sciences, 55, 2220 , doi: https://doi.org/10.1175/1520-0469(1998)055⟨2220: TMMITC⟩2.0.CO;2

Zuidema, P., Mapes, B., Lin, J., Fairall, C., & Wick, G. 2006, Journal of Climate, 19, 4531 , doi: https://doi.org/10.1175/JCLI3836.1

535   A. SPECTRAL ESTIMATE OF THE HEIGHT OF MID-TROPOSPHERIC CLEAR-SKY CONVERGENCE
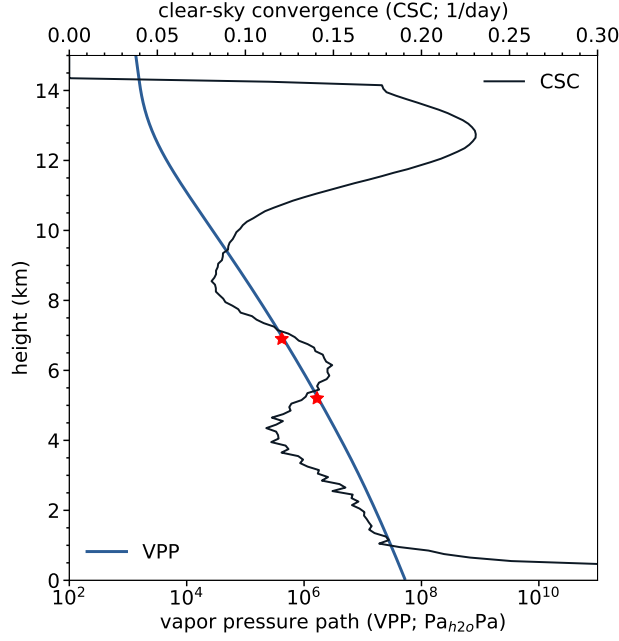

Figure 6. Clear-sky convergence in black. Vapor pressure path (Equation A3) in dark blue. The red stars denote the theoretical minimum and maximum values of VPP at the mid-tropospheric peak in CSC (Equation A4). All data are from H2O.

536   To connect with Hartmann et al. (2022), we derive the altitude of the mid-tropospheric peak in clear-sky convergence
537 (CSC) using the vapor pressure path (VPP). $\mathcal{H}$ rapidly declines around 6 km due to a drop in the abundance of
538 absorption lines in the water vapor rotation band between 0.3-1.1 m^2/kg. These absorption lines are associated with
539 strong cooling over a range of heights determined by their $\tilde{\tau} = 1$ levels. This information can be exploited to estimate
540 the height of congestus cloud tops, assuming that they overlap with the location of maximum mid-tropospheric CSC.
541   The absorption lines of water vapor are represented by the symbol $\tilde{\kappa}$. $\tilde{\kappa}$ is a fixed spectroscopic property of water
542 vapor, and its value is uniquely determined as a function of wavenumber, pressure, and temperature.

$$543 \qquad \tilde{\kappa}(\nu, p, T) \approx \tilde{\kappa}(\nu, p) = \tilde{\kappa}_{ref}(\nu, 500\text{hPa}, 260\text{K}) \frac{p}{p_{ref}} D. \tag{A1}$$

544     $\tilde{\kappa}_{ref}$ is the absorption coefficient distribution at a reference temperature (T_{ref}) and pressure (p_{ref}) of 260 K and 500
545 hPa. The roughly linear dependence of $\tilde{\kappa}$ on pressure is given by the factor p/p_{ref}, and results from pressure broadening
546 of absorption lines. Note that, for analytic tractability, we neglect the minor dependence of $\tilde{\kappa}$ on temperature. We use
547 the default RFM value for the two-stream diffisivity factor $D = 1.5$.
548   To retrieve the location of maximum mid-tropospheric CSC, we simply solve for the height of maximum cooling
549 associated with the absorption lines $\tilde{\kappa}_{ref} = 0.3\text{-}1.1$ m^2/kg. Using an approximation for the specific humidity,

$$550 \qquad q \approx \frac{R_d}{R_v} \frac{e}{p}, \tag{A2}$$

551 defining the vapor pressure path (Hartmann et al. 2022) as

$$552 \qquad \text{VPP} = \int_0^p e \, dp, \tag{A3}$$

and setting $\tilde{\tau} = 1$ (Equation 9), we arrive at a theoretical prediction for the VPP at the congestus level:

$$\text{VPP} = \frac{gR_v p_{ref}}{DR_d \tilde{\kappa}_{ref}}, \tag{A4}$$

where e is the partial pressure of water vapor and R_d and R_v are the specific gas constants of dry air and water vapor, respectively. Incredibly, the VPP is a *conserved quantity* of the mid-tropospheric CSC maximum because it is only a function of thermodynamic and spectroscopic constants. We solve Equation A4 with the idealized profiles of temperature, pressure, and humidity constructed for RFM (see Methods). This yields a height of *5.2-6.9 km* for the mid-tropospheric peak in CSC, as expected from Figure 6.

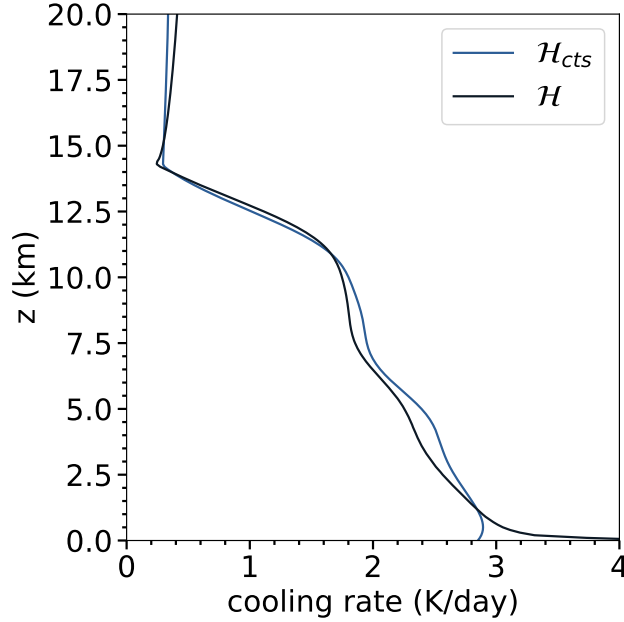## B. VALIDATION OF THE COOLING-TO-SPACE APPROXIMATION FOR WATER VAPOR

Figure 7. Comparison of the total cooling rate (black) to the cooling-to-space rate (blue) in H2O.

Figure 7 compares the full cooling rate $\mathcal{H}$ to the cooling-to-space rate $\mathcal{H}_{cts}$ from H2O. Note that the cooling rate is given in units of K/day. The main takeaway is that $\mathcal{H}_{cts}$ is in excellent agreement with $\mathcal{H}$. Both $\mathcal{H}$ and $\mathcal{H}_{cts}$ exhibit a local rapid decrease around 6 km, justifying our choice to base our analysis on $\mathcal{H}_{cts}$.